

Why the Indo-Gangetic Plain is the region with the largest NH₃ column in the globe during pre-monsoon and monsoon seasons?

Tiantian Wang¹, Yu Song¹, Zhenying Xu¹, Mingxu Liu¹, Tingting Xu^{1,2}, Wenling Liao¹, Lifei Yin¹, Xuhui Cai¹, Ling Kang¹, Hongsheng Zhang³, Tong Zhu^{1,4}

5 ¹State Key Joint Laboratory of Environmental Simulation and Pollution Control, Department of Environmental Science, Peking University, Beijing 100871, China

²Environmental College, Chengdu University of Technology, Chengdu 610059, China

³Laboratory for Climate and Ocean-Atmosphere Studies, Department of Atmospheric and Oceanic Sciences, School of Physics, Peking University, Beijing 100871, China

10 ⁴Beijing Innovation Center for Engineering Science and Advance Technology, Peking University, Beijing 100871, China

Correspondence to: Yu Song (songyu@pku.edu.cn)

Abstract. Satellite observations show a global maximum in ammonia (NH₃) over the Indo-Gangetic Plain (IGP), with a peak from June to August. However, it has never been explained explicitly. In this study, we investigated the causes of high NH₃ loading over the IGP during pre-monsoon and monsoon seasons using WRF-Chem (Weather Research and Forecasting model coupled to chemistry). IGP has relatively high NH₃ emission fluxes (0.4 t km⁻² month⁻¹) due to intensive agricultural activities and high air temperature from June to August. Additionally, low sulfur dioxide (SO₂) and nitrogen oxides (NO_x) emissions and high air temperature limit the gas-to-particle conversion of NH₃, particularly for ammonium nitrate formation. Moreover, the barrier effects of the Himalayas in combination with the surface convergence weaken the horizontal diffusion of NH₃. The high NH₃ loading over the IGP mainly results from the low gas-to-particle partitioning of NH₃ caused by low SO₂ and NO_x emissions. It contrasts to those in the North China Plain, where high SO₂ and NO_x emissions promote the conversion of gaseous NH₃ into particulate ammonium.

15
20

1 Introduction

Ammonia (NH₃) has multiple environmental implications. As the only alkaline gas in the atmosphere, it reacts with sulfuric acid (H₂SO₄) or nitric acid (HNO₃) to produce ammonium (NH₄⁺) containing aerosols (Seinfeld and Pandis, 2006), which can affect Earth's radiative balance (Abbatt et al., 2006; Adams et al., 2001) and endanger public health (Pope et al., 2002; Stokstad, 2014). In addition, NH₃ is the main form of reactive nitrogen in the environment (Reis et al., 2009), the deposition of ammonia and ammonium can cause acidification of terrestrial ecosystems and eutrophication of water bodies (Paerl et al., 2014).

25

Satellite observations (Van Damme et al., 2018; Warner et al., 2016) and ground-based measurements (Carmichael et al., 2003) have revealed that the Indo-Gangetic Plain (IGP) has the global maximum NH₃ loading, particularly from June to August. Previous studies have suggested that the high NH₃ loading over the IGP is caused by high NH₃ emissions from intensive agricultural activities (Clarisse et al., 2009; Van Damme et al., 2015b). Interestingly, satellite measurements show that the total columns of NH₃ over the IGP are much higher than those over the North China Plain (NCP), which has higher

30

NH₃ emissions fluxes (www.meicmodel.org/dataset-mix). Therefore, emissions alone might not be enough to explain the
35 high NH₃ loading over the IGP.

Apart from dry deposition and wet removal by precipitation, another main sink for NH₃ is scavenging by acidic species to
form particulate NH₄⁺. H₂SO₄ and HNO₃ resulting from the oxidation of sulfur dioxide (SO₂) and nitrogen oxides (NO_x) are
major acidic species in the atmosphere. Previous studies have confirmed that reduced SO₂ and NO_x emissions are key factors
driving the increase in NH₃ concentration (Liu et al., 2018; Yu et al., 2018; Warner et al., 2017). In addition, meteorological
40 conditions (including wind speed, precipitation, relative humidity and air temperature) also influence NH₃ loading through
various chemical and physical processes. These factors may be causing the high NH₃ loading over the IGP, but these
assumptions have not been verified in a modeling study.

In this study, we use a regional air quality model to investigate the causes of high NH₃ loading over the IGP during pre-
monsoon and monsoon seasons. This is the first study to analyze the causes of high NH₃ loading over the IGP. The
remainder of this paper is organized as follows. The air quality model and observational data are described in sect. 2. Section
45 3 analyzes the influences of several factors (including emissions, chemical conversion, and meteorological conditions) on
NH₃ loading. Among them, SO₂ and NO_x emissions over the IGP are compared to those over the NCP to clearly illustrate
their impacts on NH₃ loading. Section 4 provides concluding remarks.

2 Methods

50 2.1 WRF-Chem model and emissions inventory

WRF-Chem (Fast et al., 2006; Grell et al., 2005) version 3.6.1 was applied to investigate the cause of the high NH₃ loading
over the IGP during pre-monsoon and monsoon seasons. The simulation was performed on a domain with 30 km horizontal
resolution covering the northern part of India and parts of Pakistan, Nepal, China, and Bangladesh with 120 × 90 grid cells.
There were 23 vertical levels from the surface to the top pressure of 50 hPa. The simulations were conducted from 25 May to
55 31 August 2010 and the first 7 days (25-31 May) were treated as the spin-up period. June was considered pre-monsoon
season. July to August was considered monsoon season. The initial meteorological and boundary conditions were obtained
from the National Centers for Environmental Prediction Final Analysis with a 6 h temporal resolution. CBM-Z (Carbon
Bond Mechanism version Z) chemical mechanism (Zaveri and Peters, 1999) and MOSAIC (Model for Simulating Aerosol
Interactions and Chemistry) aerosol module (Zaveri et al., 2008) were used for modeling gas phase photochemistry and
60 aerosol processes (including nucleation, coagulation, condensation and thermodynamic equilibrium), respectively. Dry
deposition for trace gases and aerosols was treated following the methods of Wesely (1989) and Binkowski and Shankar
(1995), respectively. Wet deposition in the model includes both in-cloud and below-cloud scavenging. The below-cloud
scavenging of aerosols and trace gases was calculated based on the methods of Easter et al. (2004). More model
configurations are described in Table S1.

65 Anthropogenic emissions were obtained from the MIX inventory (Li et al., 2017), an Asian anthropogenic emissions inventory that harmonizes several local inventories using a mosaic approach. MIX uses Regional Emissions Inventory in Asia (REAS2, version 2) (Kurokawa et al., 2013) for NH₃ emissions in India.

2.2 Observational dataset

70 Atmospheric total columns of NH₃ were derived from measurements of an Infrared Atmospheric Sounding Interferometer (IASI) on board MetOp-A (<https://iasi.aeris-data.fr/NH3/>). Metop-A was launched in 2006 in a Sun-synchronous orbit with a mean local solar overpass time of 9:30 a.m. and 9:30 p.m. Only the daytime measurements have been used here, because the nighttime measurements had larger relative errors caused by the general lower thermal contrast for the nighttime overpass (Van Damme et al., 2014). It has been found that the IASI samples at the overpass time could represent the entire day, and IASI NH₃ observations are in fair agreement with the available ground-based and airborne data sets around the world (Dammers et al., 2016; Van Damme et al., 2015a). However, due to the lack of publicly available ammonia observation data sets in the IGP, previous studies have not evaluated IASI NH₃ in the IGP. This work used the ANNI-NH3-v2.2R-I retrieval product, which relied on ERA-Interim reanalysis for its meteorological inputs (Van Damme et al., 2017). The mean NH₃ column concentrations over East Asia on a 0.25° × 0.25° grid from June to August 2010 have been determined based on the relative error weighting mean method (Van Damme et al., 2014). SO₂ columns from June to August 2010 were derived from 80 the Level-3 Aura/OMI Global SO₂ Data Products (OMSO2e) (Krotkov et al., 2015). Tropospheric NO₂ columns from Ozone Monitoring Instrument (OMI) aboard NASA Aura satellite were used from June to August 2010 (http://www.temis.nl/airpollution/no2col/no2regioomimonth_qa.php).

Meteorological data at 38 sites over northern India obtained from the National Climate Data Center (<https://gis.ncdc.noaa.gov/maps/ncei/cdo/hourly>) were used to evaluate the accuracy of meteorological simulations. The 85 evaluated variables included hourly wind speed at 10 m (WS10), wind direction at 10 m (WD10), relative humidity at 2 m (RH2) and temperature at 2 m (T2). The statistical parameters included the mean bias (MB), normalized mean bias (NMB), root mean square error (RMSE) and correlation coefficient (R). In addition, air temperature at 21 sites over the NCP obtained from the National Climate Data Center were also used in this work.

2.3 ISORROPIA-II thermodynamic model

90 The thermodynamic equilibrium model, ISORROPIA-II (Fountoukis and Nenes, 2007), treating the thermodynamics of NH₄⁺-SO₄²⁻-NO₃⁻-K⁺-Ca²⁺-Mg²⁺-Na⁺-Cl⁻-H₂O aerosol system, was used to investigate the influence of air temperature on the NH₃ total columns. In this study, ISORROPIA-II was run in the “forward mode” and assuming particles are “metastable” with no solid precipitates. The chemical and meteorological data from WRF-Chem, including water-soluble ions (SO₄²⁻, NO₃⁻, NH₄⁺, Cl⁻, Na⁺) in PM_{2.5}, gaseous precursors (NH₃, HNO₃, HCl), temperature (T) and relative humidity (RH) are used 95 as the inputs of ISORROPIA-II. Using ISORROPIA-II, we simulated 20 scenarios. In these cases, air temperature of each layer increased or decreased by 10 °C synchronously, with the interval of 1 °C. Meanwhile, the other input parameters

remained the same. Then, we calculated the columnar $\epsilon(\text{NH}_4^+)$ (partitioning ratios of NH_4^+ to total ammonia (TA, $\text{TA} = \text{NH}_3 + \text{NH}_4^+$)) in each case. The columnar $\epsilon(\text{NH}_4^+)$ is the sum of the $\epsilon(\text{NH}_4^+)$ of each vertical level, but each weighted by the thickness of the layer and mass concentration of TA. Sensitivity tests were firstly conducted based on the average of the entire IGP from June to August. Then, the IGP was divided equally from northwest to southeast into three regions (namely western IGP, central IGP, and eastern IGP), and the study period was divided into the pre-monsoon season (June) and the monsoon season (July to August). Sensitivity tests were conducted for the three regions under the two seasons.

3 Results

3.1 High NH_3 emissions

IGP is a vast stretch of fertile alluvial plain spanning the banks of the Indus and Ganges Rivers and their tributaries. The main part of the IGP is located in India. The estimated NH_3 emissions in India in 2010 were 9.9 Tg, which is comparable to that in China (9.8 Tg) and accounts for about 34 % of total NH_3 emissions in Asia (Li et al., 2017). Agriculture is the largest NH_3 emitter in India, accounting for about 76 % of the total NH_3 emissions (Li et al., 2017). Agricultural NH_3 emissions mainly originate from animal husbandry and fertilizer application (Bouwman et al., 1997; Streets et al., 2003). India is the second largest N-fertilizer consumer (after China) and consumes 16.5 Tg N-fertilizers (16 % of the world's total) (FAOSTAT, 2010). In addition, there are an estimated 302 million cattle and buffalo in India (19 % of world's total), which is more than any other country (FAOSTAT, 2010). It is estimated that cattle and buffalo account for about 80 % of NH_3 emissions among livestock in India (Aneja et al., 2012).

NH_3 emissions over the IGP was 4.3 Tg in 2010 (estimated using the MIX database), which was mainly attributed to intensive agricultural practices. The IGP is known as the food bowl of India spreading across the states of Punjab, Haryana, Uttar Pradesh, Bihar, and West Bengal (blue quadrangle in Fig. 1). The total number of cattle and buffalo in the five states was estimated to be 103 million (34 % of the national total) in 2012 (GoI, 2012b). The total amount of N-fertilizer applied in the five states was estimated to be 6.9 Tg (42 % of the national total) in 2010 (GoI, 2012a). NH_3 emissions over the IGP from June to August are very high with a regional mean NH_3 emissions flux of $0.4 \text{ t km}^{-2} \text{ month}^{-1}$ (estimated using MIX database for 2010). This is consistent with satellite observations, which also show a peak of NH_3 columns over the IGP from June to August (Van Damme et al., 2015b). The peak of NH_3 emissions over the IGP might be the joint result of intensive N-fertilizer applications and high temperature. IGP has two cropping cycles including summer and winter (GoI, 2012a). June to August is one of the two main sowing periods in the IGP with a large amount of N-fertilizer applied to the cropland as base fertilizer. The monthly map of N-fertilizer application amounts from Nishina et al. (2017) shows that there are two peaks in N-fertilizer application amounts over the IGP with one in May-August, the other in November-December, which is consistent with the two cropping cycles in the IGP. In addition, the air temperature is very high over the IGP with an observed regional mean value of $30.9 \text{ }^\circ\text{C}$ from June to August 2010. Ammonia emissions increase exponentially with

temperature (Riddick et al., 2016). The high application rate of N-fertilizer and high air temperature could cause high NH₃ emissions, resulting in the high NH₃ columns.

130 The spatial distribution of mean NH₃ total columns over East Asia from June to August 2010 is shown in Fig. 1. The NH₃ columns over the IGP (7.6×10^{16} molecules cm⁻²) were about twice as large as what was observed over the NCP (4.1×10^{16} molecules cm⁻²). The NCP is also a large agricultural region (Huang et al., 2012). The regional mean NH₃ emissions flux over the NCP was 0.7 t km⁻² month⁻¹ from June to August 2010 (estimated using the MIX database), which was about 1.8 times that of the IGP. The IGP has much higher NH₃ total columns (Fig. 1) compared to the NCP, but lower NH₃ emissions
135 fluxes (Fig. S1a). Therefore, other factors might lead to the high NH₃ loading over the IGP besides high NH₃ emissions.

3.2 Low gas-to-particle conversion of NH₃

The emissions fluxes of SO₂ and NO_x (both are 0.3 t km⁻² month⁻¹) over the IGP are only about one-fourth of that over the NCP (1.1 and 1.3 t km⁻² month⁻¹) (Table 1 and Fig. S1). Besides, the satellite-derived SO₂ and NO₂ columns over the IGP (0.5 and 2.3×10^{15} molecules cm⁻²) are also much lower than that over the NCP (10.4 and 8.3×10^{15} molecules cm⁻²) (Fig.
140 S2). The relatively low SO₂ and NO_x emissions could be an important factor causing the high NH₃ columns over the IGP. In this study, we used the molar ratio (R_{emis}) of NH₃ emissions fluxes (E_A) to the sum of twice the SO₂ emissions fluxes (E_S) and NO_x emissions fluxes (E_N) to roughly represent the excess of NH₃ in the atmosphere, given by Eq. (1):

$$R_{emis} = \frac{E_A}{2 \times E_S + E_N} \quad (1)$$

The calculated R_{emis} in the IGP was 1.35, which was about 2.6 times as large as that in the NCP (0.51). We performed
145 simulations for a base case and a ‘increased SO₂/NO_x emissions’ case to investigate the impact of SO₂ and NO_x emissions on NH₃ loading. In the increased SO₂/NO_x emissions case, the emissions of SO₂ and NO_x increased 2.6 times to make R_{emis} of the IGP equal to that of the NCP.

The simulated NH₃ columns in the base case are shown in Fig. 2a. It is noted that the IASI NH₃ columns cannot be quantitatively compared to modeled NH₃ columns as the IASI NH₃ products do not provide information on the vertical
150 sensitivity (averaging kernels) to properly weight the model values. Nonetheless, the simulated regional mean NH₃ total column over the IGP from the base case of 8.8×10^{16} molecules cm⁻² is close to the satellite-derived value (7.6×10^{16} molecules cm⁻²), indicating that the model could generally capture the magnitude of NH₃ columns. Additionally, a broadly similar pattern was found in the NH₃ columns in the base run as in the satellite observations, both of which showed that NH₃ columns decrease along the IGP from northwest to southeast with the highest values in the northwestern IGP (Figs. 1 and 2a).
155 The statistical performance of the meteorological predictions at 38 sites over Northern India are presented in Table S2. The predicted T2 matched well with the observations with a correlation coefficient of 0.8 and an NMB of 4.2 %. The predicted RH2 was slightly underestimated with an NMB of -13.4 % and a correlation coefficient of 0.8. The predicted WS10 agreed reasonably well with the observations with an NMB of -5.3 %. In addition, the simulated WD10 matched well with the

observations, and both the predicted and observed dominant wind direction was SSE. The good agreement between the simulation and the observations confirms the reliability of the meteorological prediction over the simulation domain. The spatial distribution of the NH_3 total column in the increased emissions case is shown in Fig. 2b. The NH_3 total columns significantly decreased over the entire IGP, with a regional mean value of 2.5×10^{16} molecules cm^{-2} (a 72.2 % decrease compared to the base case). The surface $\epsilon(\text{NH}_4^+)$ in the base case and the increased SO_2/NO_x emissions case are shown in Fig. 2 (panels c and d, respectively). The surface $\epsilon(\text{NH}_4^+)$ in the base case was low with a regional mean value of 0.3 over the IGP. The simulated $\epsilon(\text{NH}_4^+)$ in the 2010 monsoon in Delhi was 0.38, which is close to the observed $\epsilon(\text{NH}_4^+)$ (0.39 in the 2011 monsoon season in Delhi) (Singh and Kulshrestha, 2012). In the increased SO_2/NO_x emissions case, the regional mean surface $\epsilon(\text{NH}_4^+)$ increased to 0.6 over the IGP. Significant increases in surface SO_4^{2-} and NO_3^- concentrations were also found (Fig. S3). The regional mean surface SO_4^{2-} and NO_3^- concentrations increased from 9.7 to 24.9 and from 7.2 to 20.0 $\mu\text{g m}^{-3}$, respectively. Additionally, the regional mean columnar $\epsilon(\text{NH}_4^+)$ over the IGP is 0.56 in the base case and increases to 0.87 in the increased SO_2/NO_x emissions case. This suggests that the increased SO_2 and NO_x emissions enhanced the formation of acidic species and promoted the conversion of NH_3 into NH_4^+ . The effectively reduced NH_3 total columns in the increased SO_2/NO_x emissions case indicate that low SO_2 and NO_x emissions could be the major cause of the high NH_3 loading over the IGP.

Besides the amount of acidic species, air temperature is also an important factor affecting the thermodynamic equilibrium of NH_3 between the gas phase and the particle phase. Higher air temperature limits the gas-to-particle conversion of NH_3 and enhances volatilization of NH_4NO_3 (Seinfeld and Pandis, 2006). The observed regional mean air temperature over the IGP from June to August 2010 was 30.9 °C, about 4.9 °C higher than the NCP (26.0 °C). As shown in Fig. 3a, the columnar $\epsilon(\text{NH}_4^+)$ increases as temperature decreases. A 10°C decrease in temperature results in a 0.07 increase in $\epsilon(\text{NH}_4^+)$ and a consequent 17 % decrease in NH_3 total columns. Additionally, a 10°C increase in temperature results in a 0.08 decrease in $\epsilon(\text{NH}_4^+)$ and a consequent 20 % increase in NH_3 total columns. If the temperature over the IGP drops to the temperature typical of the NCP (a 4.9 °C decrease), the NH_3 total columns over the IGP will only decrease by 10 %. In contrast, if the SO_2/NO_x emissions over the IGP increase to make the R_{emis} of the IGP equal to that of the NCP, the NH_3 column over the IGP will decrease by 72.2 %. Therefore, the low SO_2/NO_x emissions have a greater effect on causing high NH_3 columns over the IGP than the high air temperature. As shown in Figure 3c, the sensitivity of NH_3 to temperature varies in different seasons and regions. Temporally, the sensitivity of NH_3 to temperature during the monsoon season is generally higher than that during the pre-monsoon season. Spatially, the sensitivity of NH_3 to temperature is highest over the eastern IGP, followed by the central IGP and the western IGP. The difference in the sensitivity of the NH_3 to temperature may be caused by the difference of the initial $\epsilon(\text{NH}_4^+)$ and temperature.

3.3 Weak horizontal diffusion of NH_3

The IGP is surrounded by unique topography with the Himalayan range to the north and the Sulaiman range to the west. Weather on the Indian subcontinent is controlled by the low-level Indian monsoon regime from June through September

(Lawrence and Lelieveld, 2010). Fig. 4a shows the spatial distributions of surface wind flow and wind speed from June to August 2010. The dominant wind direction is southwest over the Indian peninsula and southeast over the IGP. Air mainly flows from the west coast of India and the south coast of Bengal. Surface wind speed is high on the west coast of India ($>5 \text{ m s}^{-1}$) and on the south coast of Bengal ($>4 \text{ m s}^{-1}$) but decreases from the coast inland. Mountains serve as barriers to the airflow on the surface of the Earth (Barry, 2008). Chow et al. (2013) reported that when stably stratified airflow encounters an extra-tropical mountain barrier, it is forced to rise and cool adiabatically. Consequently, higher pressure along the slope could be created, which could decelerate and block the flow. After a while, geostrophic adjustment occurs. As a result, the airflow turns left (right) in the northern (southern) hemisphere, and a barrier jet blowing parallel to the barrier is formed. As shown in Fig. 4a, the southerly airflow from the Bay of Bengal turns left when approaching the Himalayas, and then an easterly barrier jet parallel to the Himalayas is formed. The southwesterly airflow from the west coast of India also turns left when approaching the Himalayas. Similarly, wind flow at 850 hPa (Fig. 4b) also shows left-turning airflow near the Himalayas. The left-turning airflow indicates that the barrier effect of the Himalayas limits the northward movement of polluted air. Both satellite observations and the model simulation show that the high NH_3 columns over the IGP are effectively cut off by mountains to the north (Fig. 2a and Fig. S4).

As shown in Fig. 4b, an area of low geopotential height extends from Pakistan to east India following the IGP. This elongated region of low pressure is known as the monsoon trough (Bohlinger et al., 2017). It causes wind to converge over this region. The convergence of horizontal wind can be observed from wind flow at both the surface and at 850 hPa. The prevailing wind directions south and east of the IGP are southwest and southeast, respectively. As a result of convergence of horizontal winds, an area of low wind speed forms and covers most of the IGP. The regional mean surface wind speed over the IGP is $<3 \text{ m s}^{-1}$. The weak wind speed in association with the convergence weakens the horizontal advection of NH_3 and results in the accumulation of NH_3 over the IGP.

The ventilation rate (V_r) of the four edges of the IGP was used to illustrate the accumulation of an air mass over the IGP (Fig. 4d). The V_r of one edge is defined as the product of sectional area to the transport wind, given by Eq. (2):

$$V_r = AU_T \quad (2)$$

The sectional area A can be expressed as $A = ZL$, where Z is the mean planetary boundary layer (PBL) height along the edge

and L is the length of the edge. The transport wind U_T is given by
$$U_T = \frac{1}{m} \sum_{j=1}^m \left(\frac{1}{n} \sum_{i=1}^n U_{ij} \right)$$
. m and n are the number of locations along the edge and vertical levels within the PBL where the winds are measured or predicted. U_{ij} is the wind speed perpendicular to the cross-section at each height and location along the edge. The ventilation rates of the four edges of the IGP were calculated using the WRF-Chem simulation results. The total V_r of the inflow from the southern and eastern edges ($3.1 \times 10^9 \text{ m}^3 \text{ s}^{-1}$) was 64 % higher than the total V_r of the outflow from the western and northern edges ($1.9 \times 10^9 \text{ m}^3 \text{ s}^{-1}$).

The strong inflow and weak outflow indicate accumulation of the air mass over the IGP. Therefore, outward transport of NH_3 from the IGP through horizontal advection could be weak.

225 Interestingly, both relative humidity and precipitation are high over the IGP (Figs. S5), with regional mean values of 63 % and 660 mm from June to August 2010. The high relative humidity and precipitation suggest strong gas-to-particle conversion and wet scavenging of NH_3 (Seinfeld & Pandis, 2006). The observed high NH_3 loading under such a wet condition further indicates the effectiveness of other factors leading to high NH_3 loading. The simulated surface $\epsilon(\text{NH}_4^+)$ over the western, central and eastern part of the IGP were 0.11, 0.13 and 0.24 during pre-monsoon and 0.26, 0.26 0.37 during monsoon. It is not difficult to find that the surface $\epsilon(\text{NH}_4^+)$ during the monsoon season is significantly higher than that during
230 the pre-monsoon season, and the surface $\epsilon(\text{NH}_4^+)$ generally increases from northwest to southeast along the IGP. Besides, the columnar $\epsilon(\text{NH}_4^+)$ shows similar spatiotemporal variations with the surface $\epsilon(\text{NH}_4^+)$ (Figure 3b). The spatiotemporal variations of $\epsilon(\text{NH}_4^+)$ are consistent with the spatiotemporal variations of RH (Figure S5a), indicating that RH is an important factor affecting the NH_3 partitioning. The meteorological conditions in the northwest IGP are characterized by higher air temperature, lower humidity, and lower rainfall compared to the southeast IGP (Figs. 4c and S5), all of which are
235 conducive to the increase of NH_3 . Consistently, NH_3 total columns decrease from northwest to southeast along the IGP as revealed by both the satellite measurements and model simulations (Figs. 1 and 2a). However, emission fluxes of NH_3 over the northwest IGP are also obviously higher than the southeast IGP (Fig. S1). To exclude the impact of emissions on the spatial distributions of NH_3 , simulations for a “homogeneous emissions” case was performed by using WRF-Chem, where emissions of all primary pollutants over the IGP were set to their regional mean values. As shown in Fig. 5, NH_3 total
240 columns in the homogeneous emissions case still appear to decrease from northwest to southeast along the IGP. It is indicated that the meteorological factors (atmospheric diffusion, temperature, relative humidity, and precipitation) are important causes of the higher NH_3 loadings over the northwest IGP than the southeast IGP.

4 Conclusions

Satellite observations have revealed that the IGP has the global maximum NH_3 loading with a peak from June to August. Our
245 study reveals that the high NH_3 loading over the IGP appears to be the joint result of high NH_3 emissions, weak chemical loss, and weak horizontal diffusion. Intensive agricultural activities in combination with high temperature resulted in relatively high NH_3 emissions over the IGP, with a regional mean NH_3 emissions flux of $0.4 \text{ t km}^{-2} \text{ month}^{-1}$. The low SO_2 and NO_x emissions and high temperature limited the conversion of NH_3 to NH_4^+ , which is a key reason for the high NH_3 loading over the IGP. In addition, orographic and meteorological conditions also play important roles in NH_3 accumulation
250 over the IGP. The barrier effects of the Himalayas limit the northward movement of monsoon air. The low wind speed ($<3 \text{ m s}^{-1}$) in association with the surface convergence over the IGP weakens horizontal diffusion, which is conducive to the accumulation of NH_3 over the IGP.

The gas-particle partitioning plays an important role in influencing NH₃ columns. The deviation of the simulated sulfate and nitrate will cause a deviation in the simulated NH₃ by affecting NH₃ gas-particle partitioning. Thus, in addition to the NH₃ and NH₄⁺, the simulated concentrations of sulfate and nitrate are also necessary to be constrained using field observations in the future. Besides, organic species are not considered in the thermodynamic calculations in this study, because the impact of organic species on aerosol thermodynamics is still rather poorly understood (Zaveri et al., 2008; Fountoukis and Nenes, 2007). Pye et al. (2018) found that the AIOMFAC (Aerosol Inorganic–Organic Mixtures Functional groups Activity Coefficients) based equilibrium model considering inorganic-organic interactions was consistent with ISORROPIA in terms of NH₃ gas-particle partitioning. Metzger et al. (2006) found that the $\epsilon(\text{NH}_4^+)$ calculated by ISORROPIA was about 15% lower than that calculated by EQSAM2 (Equilibrium Simplified Aerosol Model) considering organic acids. Thus, the influence of organic species on the NH₃ gas-particle partitioning might be limited and will not have a significant impact on the results of this study. However, these two studies were conducted in the United States. The effects of organic species on aerosol thermodynamics in the IGP need further research in the future. Additionally, dry and wet deposition also has an important influence on NH₃ columns. Field observations of the dry and wet deposition of NH₃ and NH₄⁺ in the IGP are needed to constrain model simulations in the future.

Data availability

The IASI data used in this study was provided by the AERIS data infrastructure (<https://iasi.aeris-data.fr/NH3/>). The meteorological data used in this study was obtained from the National Climate Data Center integrated surface database (<https://gis.ncdc.noaa.gov/maps/ncei/cdo/hourly>). The anthropogenic emissions are available from MIX inventory (www.meicmodel.org/dataset-mix). The SO₂ columns were provided by the NASA Goddard Earth Sciences Data and Information Services Center (https://disc.gsfc.nasa.gov/datasets/OMSO2e_003/summary). The NO₂ columns are available from the Tropospheric Emission Monitoring Internet Service (http://www.temis.nl/airpollution/no2col/no2regioomimonth_qa.php).

275

Author contribution

Y.S initiated the investigation. T.W performed the modelling analyses. T.W, Y.S, Z.X and T.Z wrote and edited the manuscript. M.L, T.X, W.L, L.Y, X.C, H.Z and L.K contributed to discussions of the results and the manuscript.

Competing interests

280 The authors declare no competing interests.

Acknowledgements

This work was supported by the National Natural Science Foundation of China (NSFC) (91644212, 41675142 and 91837209) and the National Key R&D Program of China (2016YFC0201505).

References

- 285 Abbatt, J. P. D., Benz, S., Cziczo, D. J., Kanji, Z., Lohmann, U., and Mohler, O.: Solid ammonium sulfate aerosols as ice nuclei: A pathway for cirrus cloud formation, *Science*, 313, 1770-1773, <https://doi.org/10.1126/science.1129726>, 2006.
- Adams, P. J., Seinfeld, J. H., Koch, D., Mickley, L., and Jacob, D.: General circulation model assessment of direct radiative forcing by the sulfate-nitrate-ammonium-water inorganic aerosol system, *J. Geophys. Res. Atmos.*, 106, 1097-1111, <https://doi.org/10.1029/2000jd900512>, 2001.
- 290 Aneja, V. P., Schlesinger, W. H., Erisman, J. W., Behera, S. N., Sharma, M., and Battye, W.: Reactive nitrogen emissions from crop and livestock farming in India, *Atmos. Environ.*, 47, 92-103, <https://doi.org/10.1016/j.atmosenv.2011.11.026>, 2012.
- Barry, R. G.: *Mountain Weather and Climate*, Third Edition, Cambridge University Press, Cambridge, 2008.
- Binkowski, F. S., and Shankar, U.: The Regional Particulate Matter Model .I. Model description and preliminary results, *J Geophys Res-Atmos*, 100, 26191-26209, <https://doi.org/10.1029/95jd02093>, 1995.
- 295 Bohlinger, P., Sorteberg, A., and Sodemann, H.: Synoptic Conditions and Moisture Sources Actuating Extreme Precipitation in Nepal, *J. Geophys. Res. Atmos.*, 122, 12653-12671, <https://doi.org/10.1002/2017jd027543>, 2017.
- Bouwman, A. F., Lee, D. S., Asman, W. A. H., Dentener, F. J., VanderHoek, K. W., and Olivier, J. G. J.: A global high-resolution emission inventory for ammonia, *Global. Biogeochem. Cy.*, 11, 561-587, <https://doi.org/10.1029/97gb02266>, 1997.
- Carmichael, G. R., Ferm, M., Thongboonchoo, N., Woo, J. H., Chan, L. Y., Murano, K., Viet, P. H., Mossberg, C., Bala, R., Boonjawat, J., 300 Upatum, P., Mohan, M., Adhikary, S. P., Shrestha, A. B., Pienaar, J. J., Brunke, E. B., Chen, T., Jie, T., Guoan, D., Peng, L. C., Dhiharto, S., Harjanto, H., Jose, A. M., Kimani, W., Kirouane, A., Lacaux, J. P., Richard, S., Barturen, O., Cerda, J. C., Athayde, A., Tavares, T., Cotrina, J. S., and Bilici, E.: Measurements of sulfur dioxide, ozone and ammonia concentrations in Asia, Africa, and South America using passive samplers, *Atmos. Environ.*, 37, 1293-1308, [https://doi.org/10.1016/S1352-2310\(02\)01009-9](https://doi.org/10.1016/S1352-2310(02)01009-9), 2003.
- Chow, F. K., Wekker, S. F. J. D., and Snyder, B. J.: *Mountain Weather Research and Forecasting Recent Progress and Current Challenges*, 305 Springer, Dordrecht, 2013.
- Clarisse, L., Clerbaux, C., Dentener, F., Hurtmans, D., and Coheur, P. F.: Global ammonia distribution derived from infrared satellite observations, *Nat. Geosci.*, 2, 479-483, <https://doi.org/10.1038/ngeo551>, 2009.
- Dammers, E., Palm, M., Van Damme, M., Vigouroux, C., Smale, D., Conway, S., Toon, G. C., Jones, N., Nussbaumer, E., Warneke, T., Petri, C., Clarisse, L., Clerbaux, C., Hermans, C., Lutsch, E., Strong, K., Hannigan, J. W., Nakajima, H., Morino, I., Herrera, B., Stremme, 310 W., Grutter, M., Schaap, M., Kruit, R. J. W., Notholt, J., Coheur, P. F., and Erisman, J. W.: An evaluation of IASI-NH₃ with ground-based Fourier transform infrared spectroscopy measurements, *Atmos. Chem. Phys.*, 16, 10351-10368, <https://doi.org/10.5194/acp-16-10351-2016>, 2016.
- Easter, R. C., Ghan, S. J., Zhang, Y., Saylor, R. D., Chapman, E. G., Laulainen, N. S., Abdul-Razzak, H., Leung, L. R., Bian, X. D., and Zaveri, R. A.: MIRAGE: Model description and evaluation of aerosols and trace gases, *J Geophys Res-Atmos*, 109, 315 <https://doi.org/10.1029/2004jd004571>, 2004.
- FAOSTAT: Statistical Database of Food and Agriculture Organization of the United Nations, The Food and Agriculture Organization of the United Nations, 2010.
- Fast, J. D., Gustafson, W. I., Easter, R. C., Zaveri, R. A., Barnard, J. C., Chapman, E. G., Grell, G. A., and Peckham, S. E.: Evolution of ozone, particulates, and aerosol direct radiative forcing in the vicinity of Houston using a fully coupled meteorology-chemistry-aerosol 320 model, *J. Geophys. Res. Atmos.*, 111, <https://doi.org/10.1029/2005jd006721>, 2006.
- Fountoukis, C., and Nenes, A.: ISORROPIA II: a computationally efficient thermodynamic equilibrium model for K⁺-Ca²⁺-Mg²⁺-NH₄⁺-Na⁺-SO₄²⁻-NO₃⁻-Cl⁻-H₂O aerosols, *Atmos. Chem. Phys.*, 7, 4639-4659, <https://doi.org/10.5194/acp-7-4639-2007>, 2007.
- GoI: *Agricultural Statistics At a Glance 2012*, Ministry of Agriculture, Government of India, New Delhi, India, 2012a.
- GoI: *19th Livestock Census 2012*, Ministry of Agriculture, Government of India, New Delhi, India, 2012b.
- 325 Grell, G. A., Peckham, S. E., Schmitz, R., McKeen, S. A., Frost, G., Skamarock, W. C., and Eder, B.: Fully coupled "online" chemistry within the WRF model, *Atmos. Environ.*, 39, 6957-6975, <https://doi.org/10.1016/j.atmosenv.2005.04.027>, 2005.
- Huang, X., Song, Y., Li, M. M., Li, J. F., Huo, Q., Cai, X. H., Zhu, T., Hu, M., and Zhang, H. S.: A high-resolution ammonia emission inventory in China, *Global. Biogeochem. Cy.*, 26, <https://doi.org/10.1029/2011gb004161>, 2012.
- Krotkov, N. A., Li, C., and Leonard, P.: OMI/Aura Sulfur Dioxide (SO₂) Total Column L3 1 day Best Pixel in 0.25 degree x 0.25 degree 330 V3, Goddard Earth Sciences Data and Information Services Center (GES DISC), <https://doi.org/10.5067/Aura/OMI/DATA3008>, 2015.

- Kurokawa, J., Ohara, T., Morikawa, T., Hanayama, S., Janssens-Maenhout, G., Fukui, T., Kawashima, K., and Akimoto, H.: Emissions of air pollutants and greenhouse gases over Asian regions during 2000-2008: Regional Emission inventory in ASia (REAS) version 2, *Atmos. Chem. Phys.*, 13, 11019-11058, <https://doi.org/10.5194/acp-13-11019-2013>, 2013.
- 335 Lawrence, M. G., and Lelieveld, J.: Atmospheric pollutant outflow from southern Asia: a review, *Atmos. Chem. Phys.*, 10, 11017-11096, <https://doi.org/10.5194/acp-10-11017-2010>, 2010.
- Li, M., Zhang, Q., Kurokawa, J., Woo, J. H., He, K. B., Lu, Z. F., Ohara, T., Song, Y., Streets, D. G., Carmichael, G. R., Cheng, Y. F., Hong, C. P., Huo, H., Jiang, X. J., Kang, S. C., Liu, F., Su, H., and Zheng, B.: MIX: a mosaic Asian anthropogenic emission inventory under the international collaboration framework of the MICS-Asia and HTAP, *Atmos. Chem. Phys.*, 17, 935-963, <https://doi.org/10.5194/acp-17-935-2017>, 2017.
- 340 Liu, M. X., Huang, X., Song, Y., Xu, T. T., Wang, S. X., Wu, Z. J., Hu, M., Zhang, L., Zhang, Q., Pan, Y. P., Liu, X. J., and Zhu, T.: Rapid SO₂ emission reductions significantly increase tropospheric ammonia concentrations over the North China Plain, *Atmos. Chem. Phys.*, 18, 17933-17943, <https://doi.org/10.5194/acp-18-17933-2018>, 2018.
- Metzger, S., Mihalopoulos, N., and Lelieveld, J.: Importance of mineral cations and organics in gas-aerosol partitioning of reactive nitrogen compounds: case study based on MINOS results, *Atmos Chem Phys*, 6, 2549-2567, <https://doi.org/10.5194/acp-6-2549-2006>, 2006.
- 345 Nishina, K., Ito, A., Hanasaki, N., and Hayashi, S.: Reconstruction of spatially detailed global map of NH₄⁺ and NO₃⁻ application in synthetic nitrogen fertilizer, *Earth Syst Sci Data*, 9, 149-162, <https://doi.org/10.5194/essd-9-149-2017>, 2017.
- Paerl, H. W., Gardner, W. S., McCarthy, M. J., Peierls, B. L., and Wilhelm, S. W.: Algal blooms: Noteworthy nitrogen, *Science*, 346, 175-175, <https://doi.org/10.1126/science.346.6206.175-a>, 2014.
- 350 Pope, C. A., Burnett, R. T., Thun, M. J., Calle, E. E., Krewski, D., Ito, K., and Thurston, G. D.: Lung cancer, cardiopulmonary mortality, and long-term exposure to fine particulate air pollution, *Jama-J. Am. Med. Assoc.*, 287, 1132-1141, <https://doi.org/10.1001/jama.287.9.1132>, 2002.
- Pye, H. O. T., Zuend, A., Fry, J. L., Isaacman-VanWertz, G., Capps, S. L., Appel, K. W., Foroutan, H., Xu, L., Ng, N. L., and Goldstein, A. H.: Coupling of organic and inorganic aerosol systems and the effect on gas-particle partitioning in the southeastern US, *Atmos Chem Phys*, 18, 357-370, <https://doi.org/10.5194/acp-18-357-2018>, 2018.
- 355 Reis, S., Pinder, R. W., Zhang, M., Lijje, G., and Sutton, M. A.: Reactive nitrogen in atmospheric emission inventories, *Atmos. Chem. Phys.*, 9, 7657-7677, <https://doi.org/10.5194/acp-9-7657-2009>, 2009.
- Riddick, S., Ward, D., Hess, P., Mahowald, N., Massad, R., and Holland, E.: Estimate of changes in agricultural terrestrial nitrogen pathways and ammonia emissions from 1850 to present in the Community Earth System Model, *Biogeosciences*, 13, 3397-3426, <https://doi.org/10.5194/bg-13-3397-2016>, 2016.
- 360 Seinfeld, J. H., and Pandis, S. N.: *Atmospheric Chemistry and Physics: From Air Pollution to Climate Change*, John Wiley, New York, 2006.
- Singh, S., and Kulshrestha, U. C.: Abundance and distribution of gaseous ammonia and particulate ammonium at Delhi, India, *Biogeosciences*, 9, 5023-5029, <https://doi.org/10.5194/bg-9-5023-2012>, 2012.
- 365 Stokstad, E.: AIR POLLUTION Ammonia Pollution From Farming May Exact Hefty Health Costs, *Science*, 343, 238-238, <https://doi.org/10.1126/science.343.6168.238>, 2014.
- Streets, D. G., Bond, T. C., Carmichael, G. R., Fernandes, S. D., Fu, Q., He, D., Klimont, Z., Nelson, S. M., Tsai, N. Y., Wang, M. Q., Woo, J. H., and Yarber, K. F.: An inventory of gaseous and primary aerosol emissions in Asia in the year 2000, *J. Geophys. Res. Atmos.*, 108, <https://doi.org/10.1029/2002jd003093>, 2003.
- 370 Van Damme, M., Clarisse, L., Heald, C. L., Hurtmans, D., Ngadi, Y., Clerbaux, C., Dolman, A. J., Erisman, J. W., and Coheur, P. F.: Global distributions, time series and error characterization of atmospheric ammonia (NH₃) from IASI satellite observations, *Atmos. Chem. Phys.*, 14, 2905-2922, <https://doi.org/10.5194/acp-14-2905-2014>, 2014.
- Van Damme, M., Clarisse, L., Dammers, E., Liu, X., Nowak, J. B., Clerbaux, C., Flechard, C. R., Galy-Lacaux, C., Xu, W., Neuman, J. A., Tang, Y. S., Sutton, M. A., Erisman, J. W., and Coheur, P. F.: Towards validation of ammonia (NH₃) measurements from the IASI satellite, *Atmos Meas Tech*, 8, 1575-1591, <https://doi.org/10.5194/amt-8-1575-2015>, 2015a.
- 375 Van Damme, M., Erisman, J. W., Clarisse, L., Dammers, E., Whitburn, S., Clerbaux, C., Dolman, A. J., and Coheur, P. F.: Worldwide spatiotemporal atmospheric ammonia (NH₃) columns variability revealed by satellite, *Geophys. Res. Lett.*, 42, 8660-8668, <https://doi.org/10.1002/2015gl065496>, 2015b.
- Van Damme, M., Whitburn, S., Clarisse, L., Clerbaux, C., Hurtmans, D., and Coheur, P. F.: Version 2 of the IASI NH₃ neural network retrieval algorithm: near-real-time and reanalysed datasets, *Atmos Meas Tech*, 10, 4905-4914, <https://doi.org/10.5194/amt-10-4905-2017>, 2017.
- 380 Van Damme, M., Clarisse, L., Whitburn, S., Hadji-Lazaro, J., Hurtmans, D., Clerbaux, C., and Coheur, P. F.: Industrial and agricultural ammonia point sources exposed, *Nature*, 564, 99+, <https://doi.org/10.1038/s41586-018-0747-1>, 2018.
- Warner, J. X., Wei, Z. G., Strow, L. L., Dickerson, R. R., and Nowak, J. B.: The global tropospheric ammonia distribution as seen in the 385 13-year AIRS measurement record, *Atmos. Chem. Phys.*, 16, 5467-5479, <https://doi.org/10.5194/acp-16-5467-2016>, 2016.

- Warner, J. X., Dickerson, R. R., Wei, Z., Strow, L. L., Wang, Y., and Liang, Q.: Increased atmospheric ammonia over the world's major agricultural areas detected from space, *Geophys. Res. Lett.*, 44, 2875-2884, <https://doi.org/10.1002/2016gl072305>, 2017.
- Wesely, M. L.: Parameterization of Surface Resistances to Gaseous Dry Deposition in Regional-Scale Numerical-Models, *Atmos Environ*, 23, 1293-1304, [https://doi.org/10.1016/0004-6981\(89\)90153-4](https://doi.org/10.1016/0004-6981(89)90153-4), 1989.
- 390 Yu, F. Q., Nair, A. A., and Luo, G.: Long-Term Trend of Gaseous Ammonia Over the United States: Modeling and Comparison With Observations, *J. Geophys. Res. Atmos.*, 123, 8315-8325, <https://doi.org/10.1029/2018jd028412>, 2018.
- Zaveri, R. A., and Peters, L. K.: A new lumped structure photochemical mechanism for large-scale applications, *Journal of Geophysical Research: Atmospheres*, 104, 30387-30415, <https://doi.org/10.1029/1999jd900876>, 1999.
- 395 Zaveri, R. A., Easter, R. C., Fast, J. D., and Peters, L. K.: Model for Simulating Aerosol Interactions and Chemistry (MOSAIC), *Journal of Geophysical Research*, 113, <https://doi.org/10.1029/2007jd008782>, 2008.

Table 1. Regional Mean NH₃ Total Columns and Emissions Fluxes of NH₃, SO₂, and NO_x of the IGP and the NCP from June to August 2010.

	NH ₃ total columns ^a (molecules cm ⁻²)	Emissions fluxes ^b (t km ⁻² month ⁻¹)		
		NH ₃	SO ₂	NO _x
IGP	7.6×10 ¹⁶	0.4	0.3	0.3
NCP	4.1×10 ¹⁶	0.7	1.1	1.3

400 ^aNH₃ total columns were derived from IASI measurements

^bEmissions fluxes were estimated using the MIX database

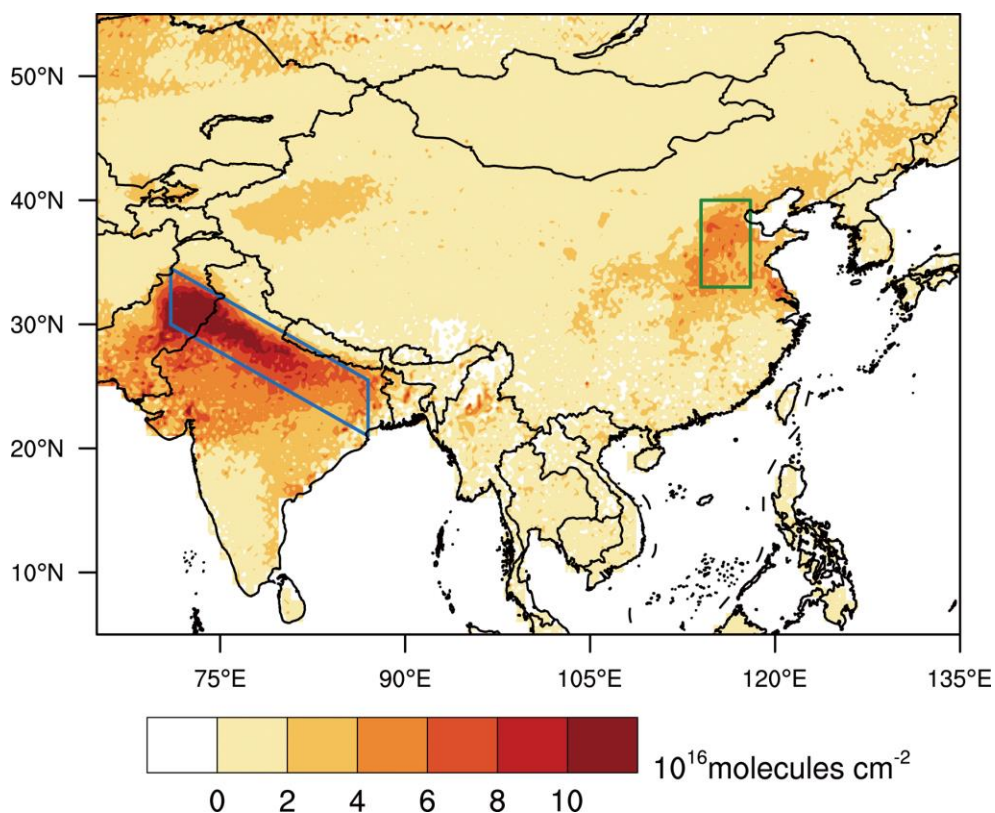


Figure 1. The spatial distribution of NH₃ total columns over East Asia from June to August 2010
 405 retrieved from IASI measurements. The blue quadrangle represents the Indo-Gangetic Plain (IGP), and
 the green quadrangle represents the Northern China Plain (NCP).

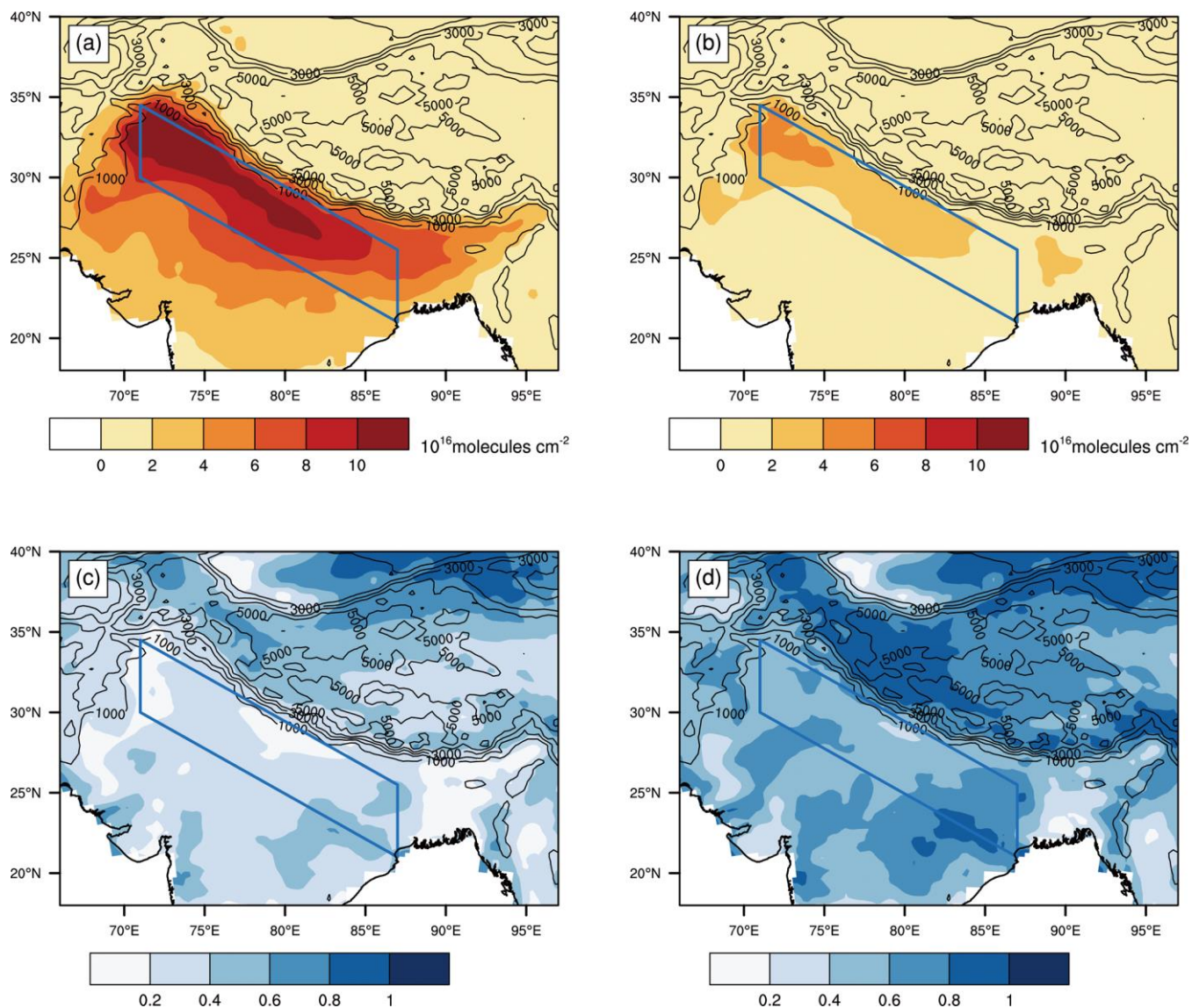
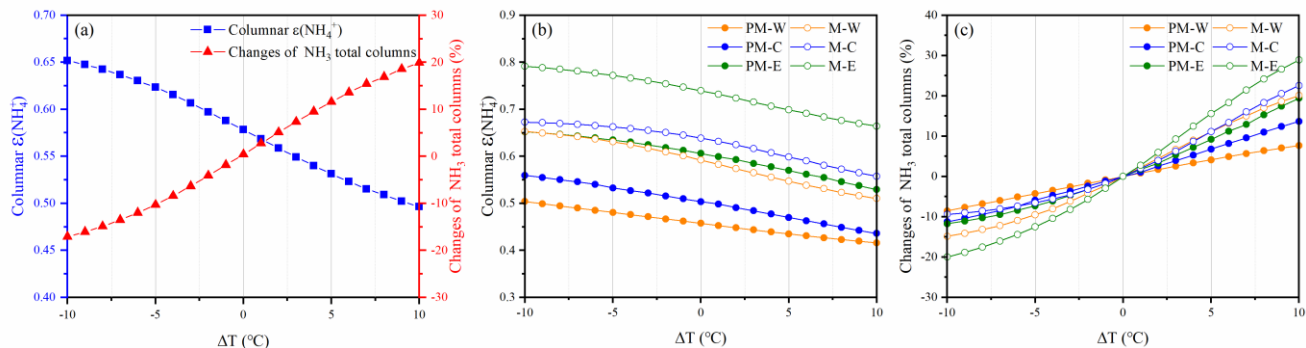


Figure 2. Spatial distributions of WRF-Chem predicted total columns of NH_3 and surface $\epsilon(\text{NH}_4^+)$ from June to August 2010. (a) and (b) are total columns of NH_3 in the base case and the increased SO_2/NO_x emissions case, respectively. (c) and (d) are surface $\epsilon(\text{NH}_4^+)$ in the base case and the increased SO_2/NO_x emissions case, respectively.



415 **Figure 3.** Columnar $\epsilon(\text{NH}_4^+)$ and changes of NH_3 total columns with the changes of temperatures predicted by ISORROPIA-II. (a) Mean columnar $\epsilon(\text{NH}_4^+)$ and changes of NH_3 total columns over the IGP from June to August 2010. (b) Columnar $\epsilon(\text{NH}_4^+)$ and (c) changes of NH_3 total columns over the western IGP during Pre-monsoon (PM-W), the central IGP during Pre-monsoon (PM-C), the eastern IGP during pre-monsoon (PM-E), the western IGP during monsoon (M-W), the central IGP during monsoon (M-C), the eastern IGP during monsoon (M-E).

420

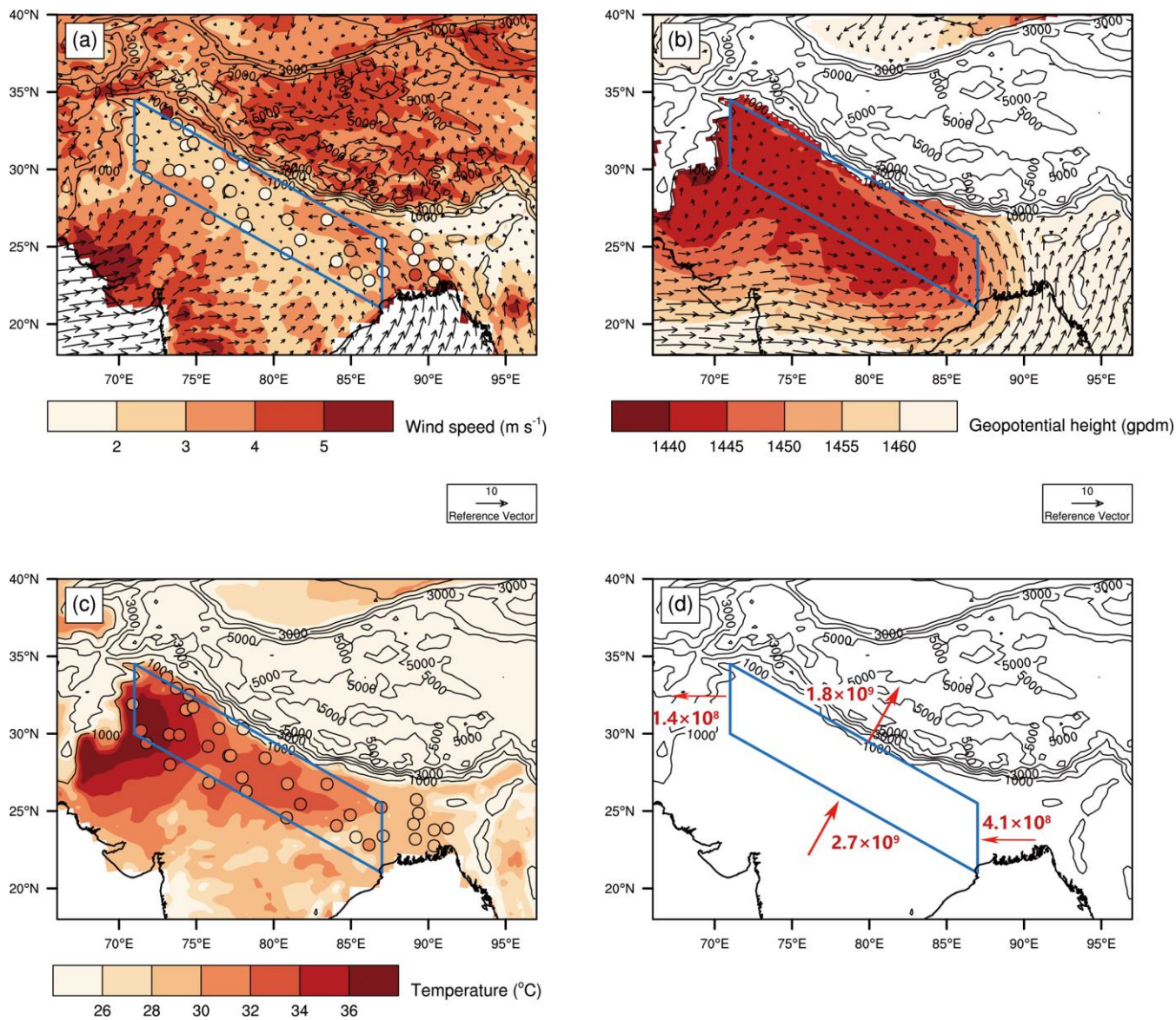


Figure 4. Spatial distributions of WRF-Chem predicted meteorological variables from June to August 2010. (a) Wind flow and wind speed at 10 m. (b) Wind flow and geopotential height at 850 hPa. (c) Air temperature at 2 m. (d) Ventilation rate ($\text{m}^3 \text{s}^{-1}$) of the four edges of the IGP. Circles in (a) and (c) show the observed wind speed at 10 m and air temperature at 2 m, respectively.

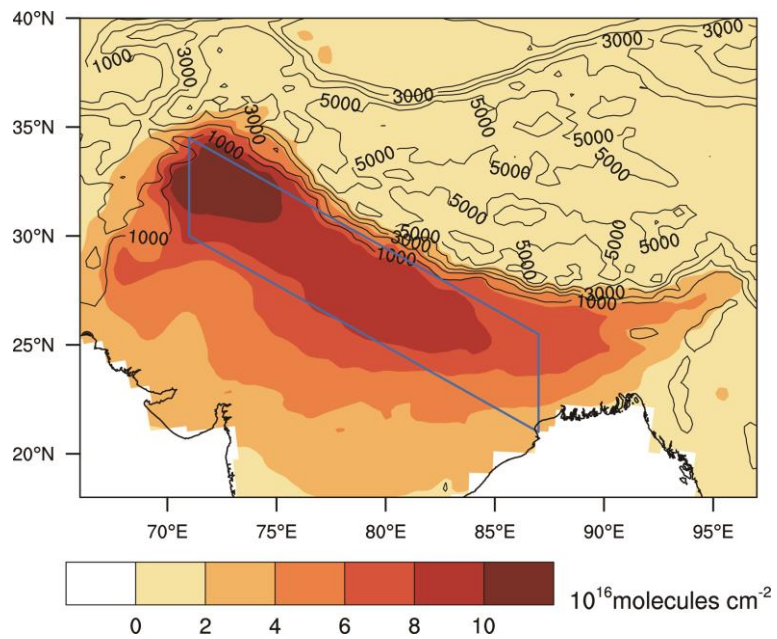


Figure 5. Spatial distributions of WRF-Chem predicted total columns of NH₃ from June to August 2010 in the homogeneous emissions case.